NANO LETTERS

pubs.acs.org/NanoLett

Letter

Engineering Heat Transport Across Epitaxial Lattice-Mismatched van der Waals Heterointerfaces

Emigdio Chavez-Angel, Polychronis Tsipas, Peng Xiao, Mohammad Taghi Ahmadi, Abdalghani H. S. Daaoub, Hatef Sadeghi, Clivia M. Sotomayor Torres, Athanasios Dimoulas, and Alexandros El Sachat*

Cite This: *Nano Lett.* 2023, 23, 6883−6891

Read Online

ACCESS | Metrics & More | Article Recommendations | Supporting Information

ABSTRACT: Artificially engineered 2D materials offer unique physical properties for thermal management, surpassing naturally occurring materials. Here, using van der Waals epitaxy, we demonstrate the ability to engineer extremely insulating thermal metamaterials based on atomically thin lattice-mismatched Bi_2Se_3/$MoSe_2$ superlattices and graphene/$PdSe_2$ heterostructures with exceptional thermal resistances (70−202 m^2 K/GW) and ultralow cross-plane thermal conductivities (0.012−0.07 W/mK) at room temperature, comparable to those of amorphous materials. Experimental data obtained using frequency-domain thermoreflectance and low-frequency Raman spectroscopy, supported by tight-binding phonon calculations, reveal the impact of lattice mismatch, phonon-interface scattering, size effects, temperature, and interface thermal resistance on cross-plane heat dissipation, uncovering different thermal transport regimes and the dominant role of long-wavelength phonons. Our findings provide essential insights into emerging synthesis and thermal characterization methods and valuable guidance for the development of large-area heteroepitaxial van der Waals films of dissimilar materials with tailored thermal transport characteristics.

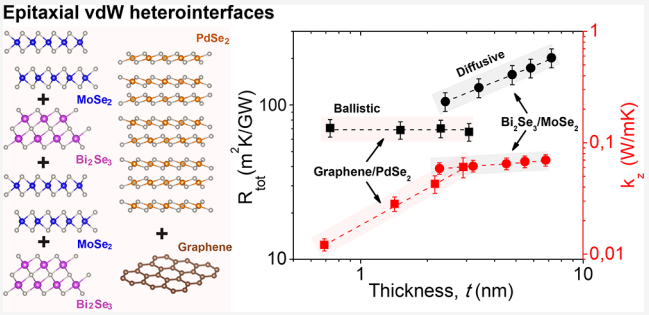

KEYWORDS: *phonon transport, thermal conductivity, frequency-domain thermoreflectance Bi_2Se_3/$MoSe_2$, graphene/$PdSe_2$*

The emergence of van der Waals (vdW) heterostructures and superlattices (SLs) has introduced new possibilities in nanoelectronics, optics, and heat transport engineering. These structures offer ultrahigh mobility, topological properties, high absorption, sensitivity, low scattering rates, and highly anisotropic properties.[1−4] Recently, researchers have proposed thermodynamically stable misfit layer compounds, vdW heterostructures, and SLs with tailored thermal transport and thermoelectric conversion properties for thermal management applications.[4−8] The periodic nature of SLs leads to the formation of new phonon modes and bandgaps due to the folding effect, which significantly modifies the phonon group velocity and thermal conductivity based on the period thickness.[9] Moreover, vdW SLs and thin films assembled from layers with structural lattice mismatch and weak vdW interactions or random interlayer rotations, could suppress phonon transport along the *c*-axis while preserving their in-plane crystallinity.[10]

Despite significant efforts toward this direction, many experimental studies have reported vdW stacks using top-down fabrication methods, such as exfoliation, which can only prepare small flakes on a micrometer scale.[8,11−13] Additionally, such flakes are most likely to have defects or contamination, which further create additional phonon scattering centers in the films. Nevertheless, recent works have demonstrated high thermal isolation across a few micrometer size exfoliated graphene/$MoSe_2$/MoS_2/WSe_2 heterostructures,[13] graphene/MoS_2 SLs,[8] and polycrystalline WS_2 films.[10] In contrast, bottom-up epitaxial techniques, such as molecular beam epitaxy (MBE), enable wafer-scale growth of high-order vdW SLs with atomically smooth and abrupt periodic interfaces.[1,14−16] The ability to control atomic layer thickness and chemical composition also allows for the precise design of the transport properties of the SLs. Moreover, vdW epitaxy offers great flexibility in integrating atomic layers of different materials such as metals, semiconductors, superconductors, or insulators, without considering lattice-matching requirements.[1,17]

Here, using wafer-scale heteroepitaxial growth, we demonstrate superior cross-plane thermal insulation based on

Received: April 5, 2023
Revised: June 27, 2023
Published: July 19, 2023

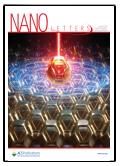

https://doi.org/10.1021/acs.nanolett.3c01280
Nano Lett. 2023, 23, 6883−6891

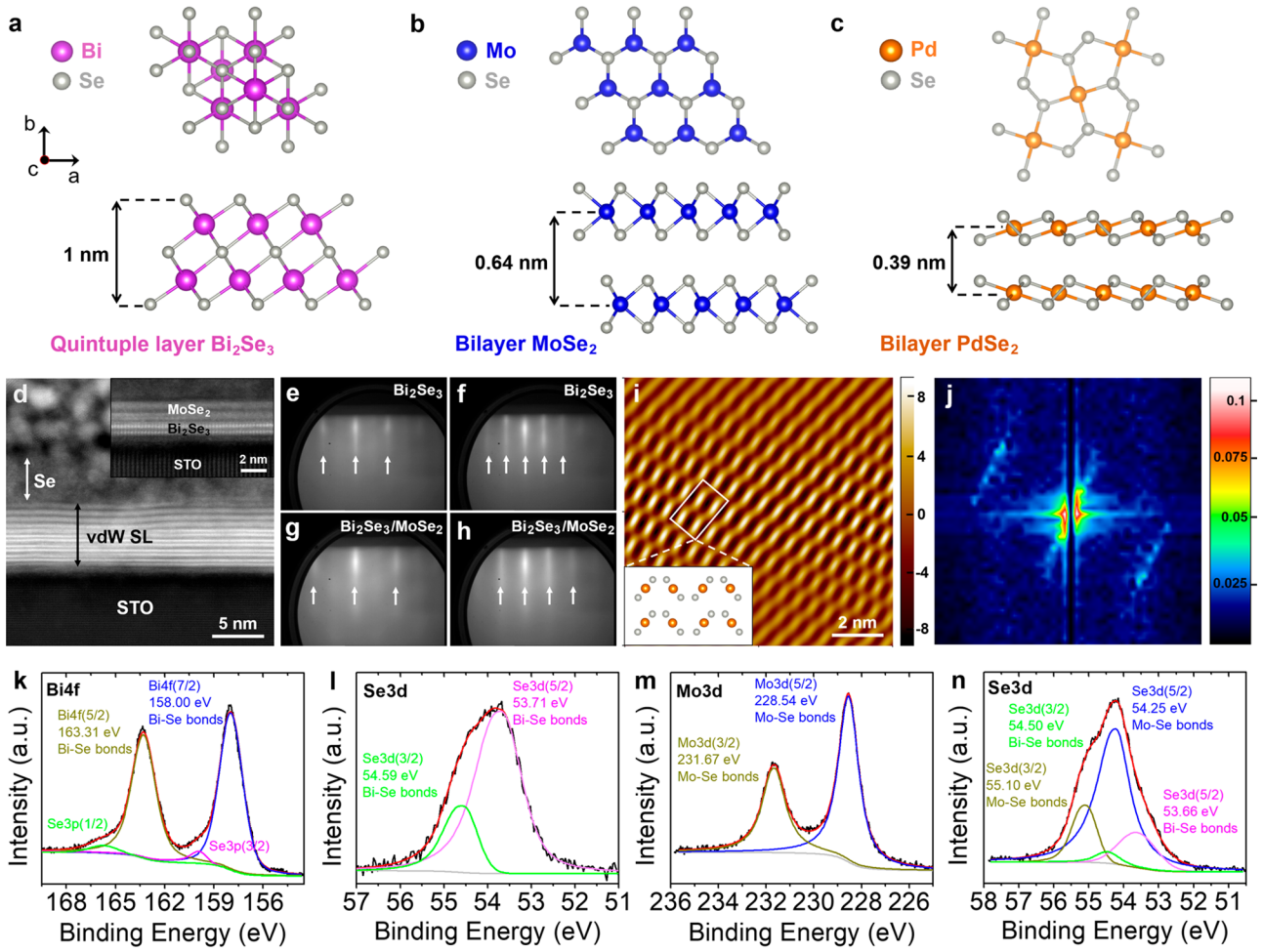

Figure 1. Structural and chemical characterization of epitaxial vdW films. Top and side views of (a) Bi_2Se_3, and (b) $MoSe_2$ and (c) $PdSe_2$ crystal structures. The purple, blue, and orange spheres represent Bi, Mo, and Pd atoms, respectively, while Se atoms are shown with gray spheres. One QL Bi_2Se_3 consists of five atoms per unit cell, such as Se−Bi−Se−Bi−Se, while each monolayer $MoSe_2$ consists of three atomic sublayers, in which Mo atoms are sandwiched between Se atoms. In $PdSe_2$, each Pd atom is connected with four Se atoms, and each Se atom is bonded with two Pd atoms and another Se atom. (d) Cross-sectional STEM images of the as-synthesized vdW $Bi_2Se_3/MoSe_2$ SLs with periods of n = 3 and n = 1 (inset) on STO substrates. After the growth, a 4 nm thick Se capping layer was deposited in situ to protect the SL from oxidation. RHEED patterns of 1 QL Bi_2Se_3 and $Bi_2Se_3/MoSe_2$ SL with period n = 1 along the (e, g) [11−20] and (f, h) [11−10] azimuths. (i) STM image of the as grown monolayer $PdSe_2$ on graphene and (j) the corresponding fast Fourier transform (FFT) image of the whole region. (k−n) XPS data of $Bi_2Se_3/MoSe_2$ SL grown on the STO substrates.

atomically thin crystalline vdW films assembled from highly dissimilar Debye temperature materials. Specifically, we directly grow high-quality lattice-matched $Bi_2Se_3/MoSe_2$ SLs and graphene/$PdSe_2$ heterostructures of varying thicknesses on different substrates, which exhibit tailored thermal transport properties at the atomic-scale. Combining contactless characterization techniques, e.g., frequency-domain thermoreflectance (FDTR) and low-frequency Raman spectroscopy, we study the acoustic and thermal properties of these epitaxial films. We focus on unraveling the impact of vibrational mismatch, phonon-interface scattering, temperature and film thickness on cross-plane thermal transport and we estimate the effective cross-plane thermal conductivity and total thermal resistance of the films taking into account all the interfacial contributions in our multilayer structures. Tight-binding phonon calculations support our experimental data and further reveal the impact of the thermal contact resistance on the thermal conduction of layered materials and the presence of different thermal transport regimes in such atomically thin 2D films. To date, only the in-plane thermal transport properties of Bi_2Se_3, $MoSe_2$, and $PdSe_2$ films have been investigated;[18−22] while such high cross-plane thermal insulation has been achieved only in polycrystalline films or exfoliated flakes.

We grew the epitaxial Bi_2Se_3 films, $Bi_2Se_3/MoSe_2$ SLs, and graphene/$PdSe_2$ heterostructures on various single-crystal substrates such as strontium titanate (STO), sapphire, and silicon carbide (SiC) by MBE, yielding 2D thin films with minimal disorder. A schematic representation of each material is shown in Figures 1a−c. The structural and chemical characterization of the samples were studied by X-ray Photoelectron Spectroscopy (XPS), low-frequency Raman spectroscopy, scanning tunnelling microscopy (STM), and high resolution scanning transmission electron microscopy (HR-STEM) measurements. HR-STEM images in Figure 1d confirmed the expected layering structures of $Bi_2Se_3/MoSe_2$ SLs, consisting of vertically stacked Bi_2Se_3 and $MoSe_2$ sublayers with atomically sharp and contamination-free interfaces. Reflection high-energy electron diffraction (RHEED) patterns show that $MoSe_2$ and Bi_2Se_3 layers are repeatedly grown highly oriented on top of each other despite

https://doi.org/10.1021/acs.nanolett.3c01280
Nano Lett. 2023, 23, 6883−6891

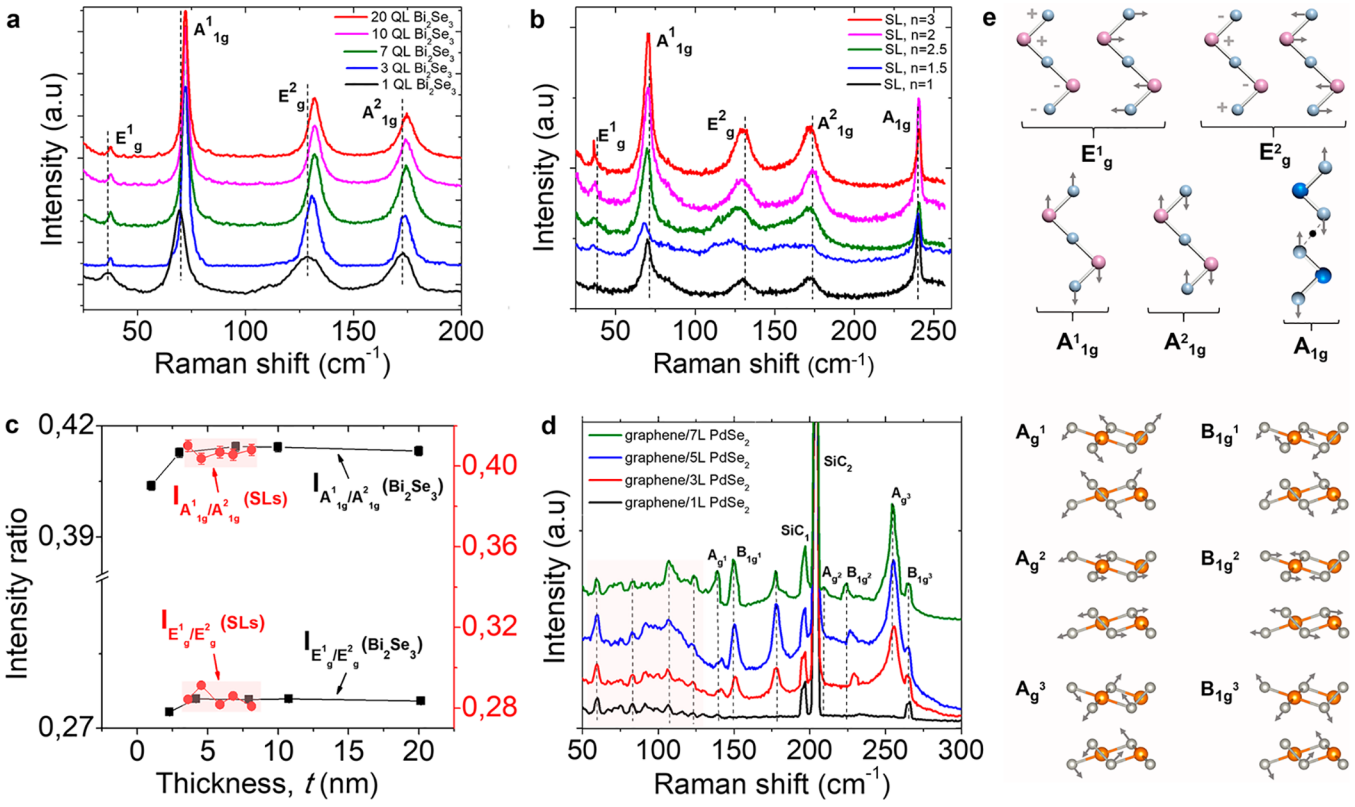

Figure 2. Low-frequency Raman spectroscopy in epitaxial vdW films. Raman scattering spectra in (a) Bi_2Se_3 films of different thickness and (b) Bi_2Se_3/$MoSe_2$ SLs. (c) Ratios of the Raman intensities for the out-of-plane (IA^1_{1g}/IA^2_{1g}) and in-phase shear modes (IE^1_g/IE^2_g) versus film thickness for the case of Bi_2Se_3 films (black squares) and Bi_2Se_3/$MoSe_2$ SLs (red circles). (d) Low-frequency Raman scattering spectra in graphene/$PdSe_2$ heterostructures of different thicknesses. The red-shaded area shows the frequency region where the Raman-inactive modes are detected. (e) Atomic displacements (gray arrows) of all the Raman modes detected in Bi_2Se_3 films, Bi_2Se_3/$MoSe_2$ SLs, and graphene/$PdSe_2$ heterostructures. The purple, blue, and orange spheres represent Bi, Mo and Pd atoms, respectively, while Se atoms are shown with gray spheres.

their large lattice mismatch (~20%) (see Figure S1 in the Supporting Information (SI)). The RHEED patterns of one quintuple layer (QL) Bi_2Se_3 and Bi_2Se_3/$MoSe_2$ heterostructures (Figure 1e–h) show the difference in the relative positions of the streaks, which reflects the large lattice mismatch between Bi_2Se_3 and $MoSe_2$ at room temperature.

Figures 1k–n displays in situ XPS data for the Bi_2Se_3 thin films and Bi_2Se_3/$MoSe_2$ heterostructures. The binding energies of the Bi $4f_{7/2}$ and Se $3d_{5/2}$ core levels for 1 QL Bi_2Se_3 grown directly on STO were 158.00 and 53.71 eV, respectively, in agreement with previous reports.[23] After 2 monolayers $MoSe_2$ growth, the Mo $3d_{5/2}$ and Se $3d_{5/2}$ peak positions at 228.54 and 54.25 eV, respectively, indicated Mo–Se bonds and agreed well with the $MoSe_2$ formation.[24] The Se 3d peak in Figure 1n is deconvoluted into four peaks to consider two types of bonds, namely, Bi–Se and Mo–Se bonds, keeping the Se $3d_{5/2}$-$3d_{3/2}$ spin–orbit splitting fixed at 0.86 eV. The two distinct Se environments suggest Bi_2Se_3 and $MoSe_2$ formation rather than the formation of a mixed Bi–Mo–Se compound. The latter is reinforced by the fact that the Bi $4f_{7/2}$ peak position remains the same after $MoSe_2$ film growth (Figure S2). The XPS spectra of pristine graphene and graphene/$PdSe_2$ heterostructures are shown in Figure S3.

Next, we systematically study the phonon properties of Bi_2Se_3 films, Bi_2Se_3/$MoSe_2$ SLs, and graphene/$PdSe_2$ heterostructures, using low-frequency Raman spectroscopy. Figure 2a shows the Raman spectra of Bi_2Se_3 films of varying thickness, where all of the out- and in-plane Raman active optical modes are observed. Specifically, the E^1_g, E^2_g, A^1_{1g}, and A^2_{1g} modes are detected at ~37 cm^{-1}, ~32 cm^{-1}, ~71 cm^{-1}, and ~173 cm^{-1}, respectively, in agreement with previous studies.[25,26] Both out-of-plane modes (A^1_{1g}, A^2_{1g}) show a pronounced red shift (about 2.7 cm^{-1}) as the thickness decreases; while the in-plane modes (E^1_g, E^2_g) are red-shifted with decreasing thickness of about 1.7 and 3.5 cm^{-1}, respectively (see also Figure S11a). We note that the A^1_{1g} is more sensitive with thickness because it reflects the out-of-plane vibrations of the Se and Bi atoms.[26] We also observe a broadening of the E^2_g mode as the film thickness decreases (Figure 2a), in agreement with previous reports,[26] suggesting that the layer-to-layer stacking strongly affects the interlayer bonding. In SLs (Figure 2b) except of the Raman modes that correspond to Bi_2Se_3, we detect the A_{1g} mode in the spectral range of 240.1–241.1 cm^{-1}, which confirms the existence of $MoSe_2$ layers.[27,28] In Figure 2c we plot the ratios of the Raman intensities for the out-of-plane (IA^1_{1g}/IA^2_{1g}) and in-phase shear modes (IE^1_g/IE^2_g) of the adjacent layers versus thickness for the case of Bi_2Se_3 films and Bi_2Se_3/$MoSe_2$ SLs for direct comparison. We find that in Bi_2Se_3 films, both IA^1_{1g}/IA^2_{1g} and IE^1_g/IE^2_g ratios decrease with decreasing thickness of less than 3 nm, in agreement with a previous study.[26] In the SLs, the ratios IA^1_{1g}/IA^2_{1g} and IE^1_g/IE^2_g are similar to those calculated in Bi_2Se_3 films and remain almost constant with decreasing period.

In graphene/$PdSe_2$ heterostructures, we detected 6 main peaks in the high-frequency region (>130 cm^{-1}) that belong to A^1_g, B^1_{1g}, A^2_g, B^2_{1g}, A^3_g, and B^3_{1g} phonon modes of $PdSe_2$ (Figure

https://doi.org/10.1021/acs.nanolett.3c01280
Nano Lett. 2023, 23, 6883–6891

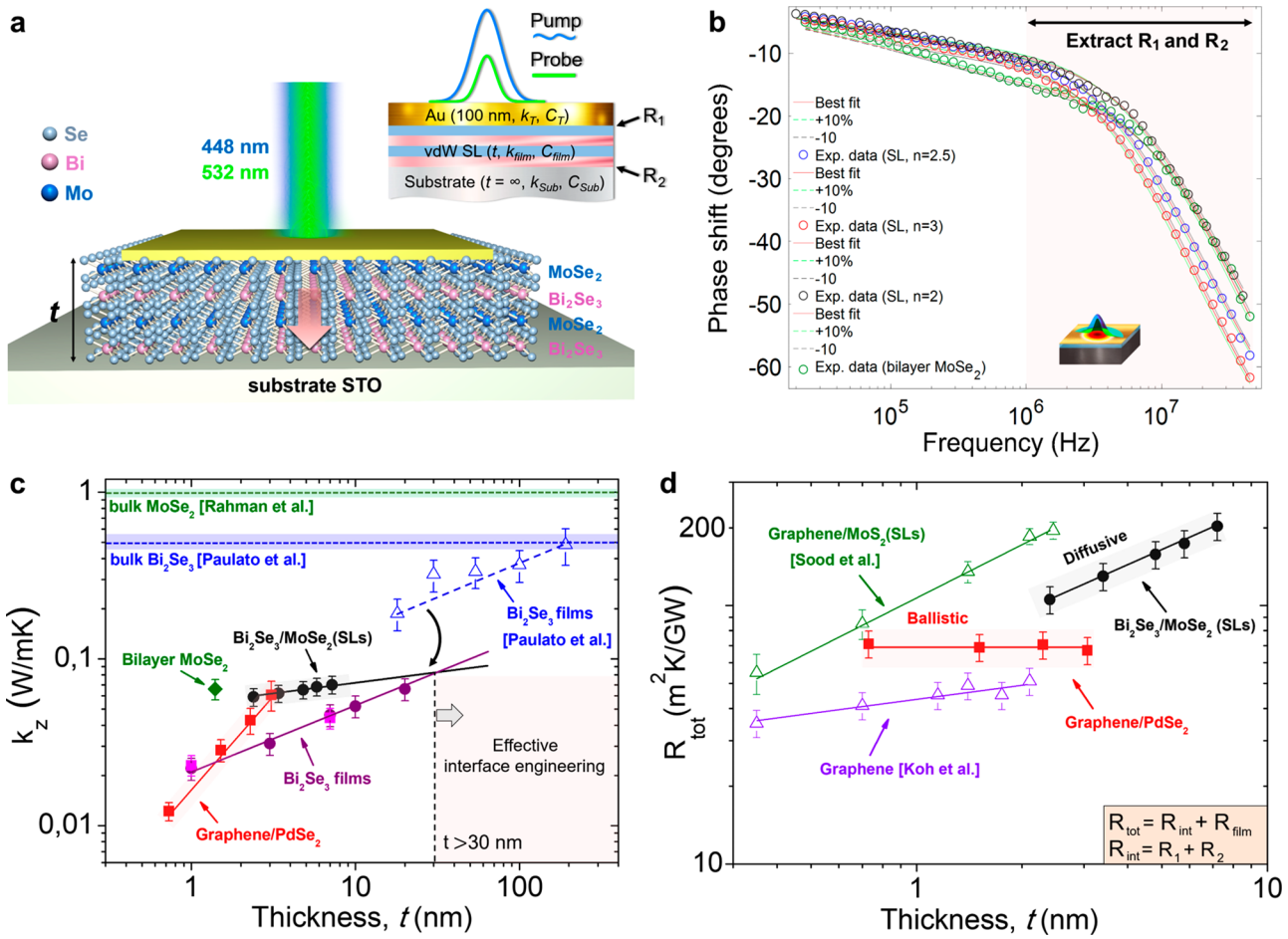

Figure 3. Thermal conductivity and interfacial heat transport measurements. (a) Schematic illustrations of the FDTR technique and the multilayer system of the SLs. (b) Typical FDTR data measured in bilayer $MoSe_2$ (green circles) and $Bi_2Se_3/MoSe_2$ SLs with periods n = 2, 2.5, and 3 and the corresponding best model fits in the entire frequency range (20 kHz to 45 MHz). (c) Cross-plane thermal conductivity versus film thickness measured in bilayer $MoSe_2$ (green solid rhomb), $Bi_2Se_3/MoSe_2$ SLs (black circles), graphene/$PdSe_2$ heterostructures (red squares), and Bi_2Se_3 films on STO (purple circles) and sapphire (pink squares) substrates. The blue triangles show previously reported k_z values measured in thicker Bi_2Se_3 films.[20] By extrapolating the k_z trends, we find the minimum film thickness from which phonon-interface scattering starts to have a strong impact on cross-plane heat dissipation, i.e., $k_{z(SLs)} < k_{z(Bi2Se3)} < k_{z(MoSe2)}$. (d) Total thermal resistance, $R_{tot} = R_{int} + R_{film}$, of the $Bi_2Se_3/MoSe_2$ SLs (black solid circles) and graphene/$PdSe_2$ heterostructures (red squares) versus film thickness. The uncertainty of the estimated R_{tot} was calculated on the basis of the error propagation for the input parameters. Total thermal resistance measurements in Au/graphene/SiO_2[49] (purple open triangles) and Al/graphene-MoS_2 (SLs)/SiO_2[8] (green open rhombs) are included for comparison. The colored lines in parts c and d are guides for the eye.

2d). These modes can be attributed to the intralayer vibrations of $PdSe_2$. The Raman peak positions of all phonon modes showed a red shift with increasing the number of layers, in agreement with previous CVD grown $PdSe_2$ films.[29,30] Interestingly, the intralayer vibration at 149.1 cm^{-1}, originating from the intralayer Se−Se bonds, exhibits sufficiently strong Raman intensity in 3, 5, and 7L $PdSe_2$, indicating its strong coupling to the electronic states.[29] Furthermore, we observe Raman-inactive modes in the frequency region between 50−130 cm^{-1}, which are activated due to the breakdown of translation symmetry in few layers, as has been recently shown.[30,31] The phonon modes detected in the frequency region between 100 and 300 cm^{-1} are also consistent with the ones found in exfoliated graphene/$PdSe_2$ heterostructures.[32] Finally, the two Raman peaks, SiC_1 and SiC_2 at 196.6 and 204.3 cm^{-1}, respectively, originated from the undoped SiC substrate.[33] We note that the mode A_g^2 is not very visible, because it partially overlaps with the SiC_2 mode.

Thermal measurements were performed using a custom-built FDTR setup, which combines simultaneous measurements of cross-plane thermal conductivity (k_z) and interface thermal conductance.[34,35] For the case of SLs, our multilayer structures consist of Au (transducer)/SLs/substrate stacks (Figure 3a). The effective k_z and the interface thermal resistances between Au/SLs (R_1) and SLs/substrate (R_2) were obtained for each SL following a multilayer three-dimensional heat diffusion model.[36] Material properties required for the model were the thickness (t), the volumetric heat capacity (C), R_1, R_2, and k_z. The k_z and C of Au as well as the volumetric specific heat of Bi_2Se_3 and $MoSe_2$ were taken from the literature.[37,38] To estimate the unknown parameters (k_z, R_1, and R_2), first we quantified the sensitivity of the recorded phase signal to different parameters (Figure S4) using our previously reported methodology.[34,35]

Examples of the recorded phase signal and the corresponding best model fits are shown in Figure 3b. To extract the k_z of each SL from a single measurement, we followed the same

https://doi.org/10.1021/acs.nanolett.3c01280
Nano Lett. 2023, 23, 6883−6891

approach that used in previous works,[34−36,39] and supported by the sensitivity analysis. First, we extract k_z by fitting the experimental data in a low frequency range (20 kHz to 1 MHz), where the sensitivity to R_1, R_2, and C is negligible. Then, we fix k_z and fit the high frequency range (1−45 MHz) to estimate R_1 and R_2. The same procedure was followed to extract k_z, R_1, and R_2 for all films. The sensitivity analysis and FDTR data for the case of graphene/$PdSe_2$ are shown in Figures S5 and S6, respectively. In Figure S9, we also show all the interface thermal resistance values, $R_{int} = R_1 + R_2$, where $R_1 = 1/G_{12}$ and $R_2 = 1/G_{23}$ extracted by the FDTR experiments and compare them with previous reports.

In SLs, we found that k_z slightly increases with increasing thickness with values between 0.059−0.07 W/mK (Figure 3c). However, in graphene/$PdSe_2$ heterostructures, we found a strong thickness-dependent k_z. Specifically, the k_z increased by a factor of 6 with increasing thickness of the $PdSe_2$ from one to seven layers. To confirm the robustness of our approach to measuring the intrinsic k_z of thin films, we performed FDTR measurements in Bi_2Se_3 films of different thicknesses on both STO and sapphire substrates. We found that the k_z increases by a factor of 5 with increasing thickness from 1 to 20 QL. The excellent agreement in k_z values is shown in Figure 3c.

The weak thickness dependence of k_z in SLs can be understood considering both interface-phonon scattering and size effects. Considering diffusive thermal transport, it is likely that short-wavelength thermal phonons are scattered by multiple Bi_2Se_3−$MoSe_2$ interfaces with increasing film thickness, thus reducing their contribution to cross-plane thermal transport. However, as the volume fraction of the SLs constituents increases, more long-wavelength phonons are allowed to propagate and contribute to k_z until they are scattered at the sample boundaries. These opposite effects resulted in the suppressed thickness-dependent k_z trend presented in Figure 3c. Therefore, despite the influence of phonon-interface scattering on k_z, the increase of k_z with increasing thickness in SLs indicates that in this thickness range, finite size effects are still dominant. This is in agreement with previous studies that showed that the transmission of phonons across short-period AlN/GaN[40] and SiGe[41,42] SLs strongly depends on the phonon wavelength, suggesting that long-wavelength phonons are the dominant carriers of heat. Molecular dynamics simulations have also shown that the k_z of SLs with lattice-mismatched interfaces increases monotonically with period length.[43]

However, the absence or limited mismatched interfaces in pure Bi_2Se_3 and graphene/$PdSe_2$ allow the majority of the thermally excited phonons to contribute to cross-plane thermal transport; i.e., k_z is limited mainly by finite size effects. This is reflected in the different rates of the k_z increase observed in Figure 3c. In particular, for the same thickness range, in Bi_2Se_3/$MoSe_2$ SLs we found only a 28% increase in k_z with increasing thickness, while in Bi_2Se_3 and graphene/$PdSe_2$ films, it was about 42% and 68%, respectively. We note that to study coherent and incoherent effects in SLs, the volume fraction of the constituents and total thickness of the films should remain constant while the thickness of each layer in a period must be adjusted to vary the interface density.[16] Therefore, in our SLs, the apparent linear scale of k_z versus period is not sufficient to conclude if phonons propagate coherently across the film thickness. For instance, previous calculations showed that despite the linear k_z increase with thickness, the lattice-mismatch destroys the Bragg reflection conditions and phonons are diffusely scattered at interfaces, thus losing their coherency.[43]

To understand whether coherent or incoherent thermal transport occurs, we quantify the impact of cross-plane ballistic phonon transport on the total thermal resistance in our epitaxial films. Specifically, we estimate the total thermal resistance per unit area, R_{tot}, which can be written as the sum of the combined interface thermal resistance, $R_{int} = R_1 + R_2$, and volumetric cross-plane thermal resistance, $R_{film} = t/k_z$.[34,44] From these calculations, we found that in the SLs R_{tot} is linearly proportional to the total thickness (or number of periods, n), such that $R_{tot,\ n=3} > R_{tot,\ n=2,5} > R_{tot,\ n=2} > R_{tot,\ n=1,5} > R_{tot,\ n=1}$ (Figure 3d). Furthermore, we observe that R_{int} increases with increasing thickness (Figure S9), in agreement with previous thermal resistance measurements in short-period SLs.[8,40] We note that the large lattice-mismatch between Bi_2Se_3 and $MoSe_2$ (~20%) most likely enhances the phonon-interface scattering and further contributes to the increased values of R_{tot}. This is in agreement with previous studies that showed that lattice-mismatched interfaces exhibit reduced interface thermal conductance and phonon transmission due to the increased lattice disorder.[45,46]

However, in graphene/$PdSe_2$ heterostructures, R_{tot} remains constant with increasing the thickness of $PdSe_2$ from 1 to 7 layers. In fact, the different slopes in Figure 3d suggest different thermal transport regimes. The similar values of R_{tot} in graphene/$PdSe_2$ indicate strong ballistic thermal transport taking into account the variations of both R_{int} (see Figure S9) and R_{film} with thickness as we show later on. We note that cross-plane ballistic transport in graphene/$PdSe_2$ is favorable since SiC/graphene interfaces exhibit excellent interfacial coupling and superior cross-plane thermal conductance,[47,48] which reduce interfacial phonon scattering. Similarly, cross-plane ballistic or quasi-ballistic thermal transport has been found in graphene,[49] MoS_2,[44] and $PtSe_2$[34] thin films. However, the increased values of R_{tot} with increasing thickness observed in SLs indicate additional phonon scattering (diffusive regime). We attribute this result to the scattering of high-frequency phonons (>58 THz − Debye frequency of Bi_2Se_3) at multiple Bi_2Se_3/$MoSe_2$ interfaces i.e., lattice mismatch destroys the coherence of high-frequency phonons. Note that the relatively high Debye temperature ratio between Bi_2Se_3 and $MoSe_2$ (see calculations in Figure S13a,b) further suggests the formation of high-interface thermal resistance heterointerfaces.

To further support the previous analysis and exclude the top and bottom interfacial contributions to R_{tot}, we plot the variations of the volumetric thermal resistance component versus thickness (see Figure S12). In the SLs, we observe that R_{film} is increasing by more than a factor of 2 as the thickness increases from 1.4 to 7.2 nm, which suggests phonon diffusive scattering at interfaces. Notably, in ultrathin graphene/$PdSe_2$ stacks, we observe that R_{film} remains almost constant ~54 m^2 K/GW with thickness, i.e., ballistic phonon transport. The similar thermal resistance trends observed in Figure 3d and Figure S12 confirmed the distinct nature of cross-plane heat transport between graphene/$PdSe_2$ and Bi_2Se_3/$MoSe_2$ SLs. Similarly, Sood et al. using density functional theory (DFT) calculations have estimated a ballistic resistance of 10 m^2 K/GW in MoS_2 films in the limit of 2−3 monolayers.[44] The significant contribution of the R_{film} component to the R_{tot} in all the epitaxial films suggests that interfacial effects do not entirely govern cross-plane thermal transport.

https://doi.org/10.1021/acs.nanolett.3c01280
Nano Lett. 2023, 23, 6883−6891

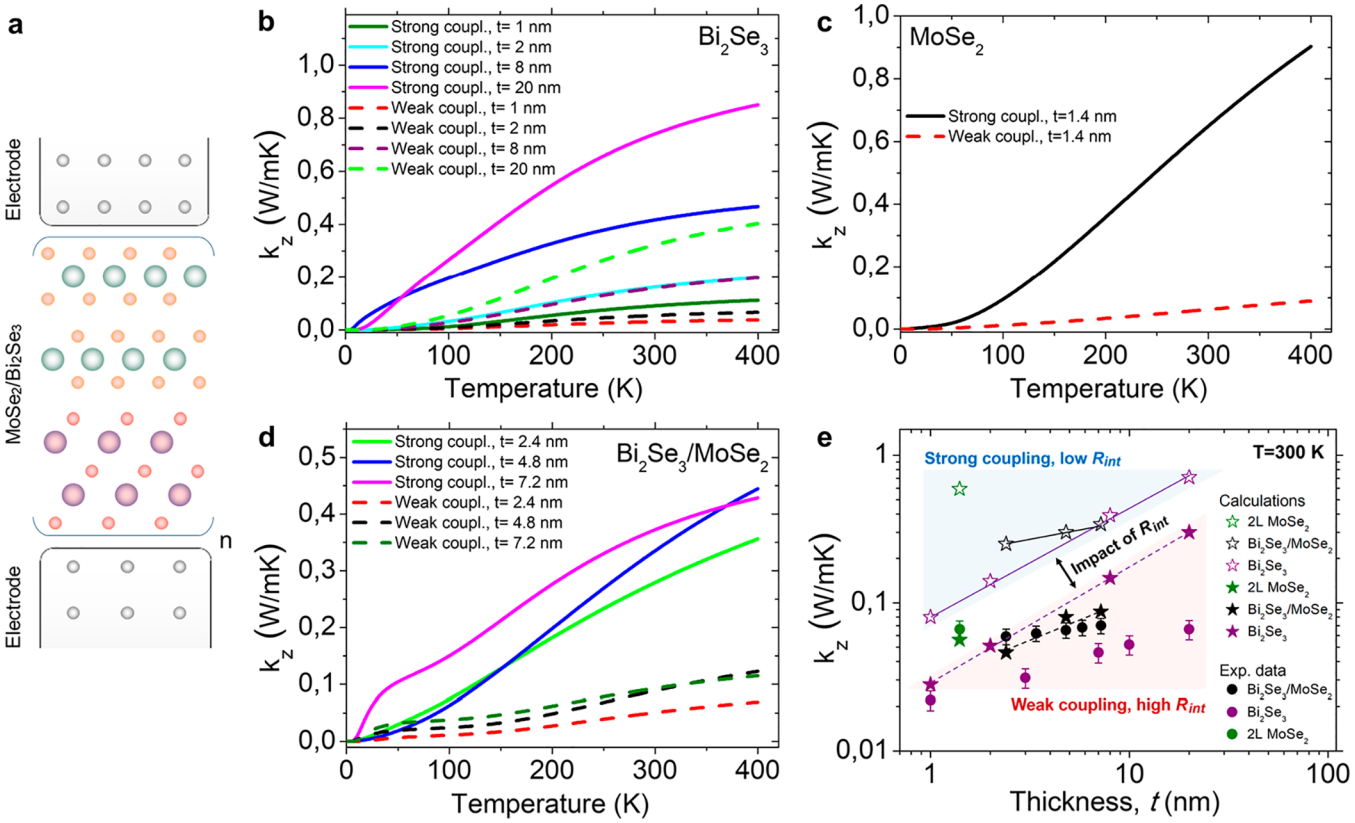

Figure 4. Tight-binding phonon calculations. (a) Schematic structure of a $Bi_2Se_3/MoSe_2$ vdW heterostructure between electrodes. The calculated cross-plane thermal conductivity of (b) Bi_2Se_3, (c) bilayer $MoSe_2$, and (d) $Bi_2Se_3/MoSe_2$ heterostructures of different thicknesses as a function of temperature (0−400 K) considering weak and strong coupling of the vdW films with the electrodes. (e) The calculated room temperature cross-plane thermal conductivity as a function of thickness for $MoSe_2$, Bi_2Se_3, and $Bi_2Se_3/MoSe_2$ heterostructures with weak (solid star symbols) and strong (open star symbols) coupling with the electrodes. The experimental k_z values for $MoSe_2$, Bi_2Se_3, and $Bi_2Se_3/MoSe_2$ are shown with green, purple, and black solid circles in (e) for direct comparison with the calculations. The difference in the calculated values indicated in blue and red shaded areas in (e) show the importance of quantifying interfacial thermal transport in vdW films bonded to a substrate.

To gain further insight into the influence of phonon-interface scattering on cross-plane thermal conductance, we developed a tight-binding model[50] and calculated the transmission coefficients of phonons with different frequencies traversing through $MoSe_2$, Bi_2Se_3, and $Bi_2Se_3/MoSe_2$ heterostructures from one metallic electrode to the other (Figure 4a). The DFT calculations indicate that the Debye frequencies of $MoSe_2$ and Bi_2Se_3 are 5.8 THz and 11.6 THz, respectively.[51,52] We adjusted the parameters of our tight-binding model to obtain similar Debye frequencies for both materials and took into account the lattice-mismatch between the heterostructure layers by selecting different coupling strengths and configurations between $MoSe_2$ and Bi_2Se_3 (see SI Section 4 and Figure S13).

In these calculations, the $Bi_2Se_3/MoSe_2$ heterostructures, which are considered new crystals, show modified phonon dispersions and vibrational properties. The large mismatch and weak phonon coupling between the Bi_2Se_3 and $MoSe_2$ layers lead to localized phonon modes and suppressed thermal conductance. Classically this can be effectively regarded as strong suppression of phonon transport at the interfaces, as we discussed above. To account for the effect of contact resistance to electrodes on the overall thermal conductance, we considered two scenarios with weak and strong couplings to electrodes. We note that although weak and strong coupling to electrodes in our nonequilibrium Green's function (NEGF)-based phonon transport calculations are not directly equivalent to large or small interface resistance, respectively, they are closely related. For example, when the coupling to the electrode is weakened, the width of the phonon transport resonances decreases, leading to lower thermal conductance.

Figure 4b−d shows the calculated k_z of different thickness Bi_2Se_3, $MoSe_2$, and $Bi_2Se_3/MoSe_2$ heterostructures as a function of temperature. The k_z increases with increasing temperature and starts to saturate at higher temperatures. Specifically, in films with strong coupling to electrodes, the width of the phonon transmission resonances increases, leading to faster increase in the thermal conductivity with temperature. Figure 4e shows the room temperature k_z as a function of film thickness, which is in good qualitative agreement with the experimental data when we consider strong coupling between films and electrodes (blue-shaded area). Specifically, the k_z trends follow a similar order to that in the experiment, and unlike Bi_2Se_3, the k_z in the SLs varies slowly with thickness. When we consider a weak coupling to the electrodes, the calculated absolute k_z values are in much better quantitative agreement with the experiments (red-shaded area). This suggests that R_{int} is increased when the films are weakly coupled with the top and bottom electrodes, confirming the relatively high R_{int} values obtained from FDTR experiments (Figure S9). These results highlight the role of thermal contact resistance in cross-plane thermal conductivity of ultrathin layered materials.

https://doi.org/10.1021/acs.nanolett.3c01280
Nano Lett. 2023, 23, 6883−6891

In summary, we have successfully developed highly insulating thermal metamaterials based on ultrathin epitaxial vdW films comprising of dissimilar atomically thin layers of 2D semiconductors ($MoSe_2$ and $PdSe_2$), the 3D topological insulator Bi_2Se_3 and monolayer graphene. The following phonon engineering approach was based on creating vertical vdW SLs consisting of atomic layers with large acoustic and structural lattice mismatch. In particular, short period Bi_2Se_3/$MoSe_2$ superlattices can be used to achieve a superior thermal resistance up to 202 m^2K/GW and ultralow cross-plane thermal conductivity down to 0.059 W/mK. We attribute this result to the large lattice mismatch between the constituent layers of the superlattices that boosts phonon-interface scattering and suppress cross-plane heat dissipation. Conversely, graphene/$PdSe_2$ heterostructures exhibit a strong thickness-dependent k_z and a constant total thermal resistance of 70 m^2K/GW (ballistic transport), mainly due to the excellent interfacial thermal coupling between graphene-SiC interfaces. Given the sub-3 nm thickness of these heterostructures, their k_z at room temperature are estimated between 0.012 and 0.06 W/mK. Our tight-binding calculations align well with the experimental results and further uncover the impact of interfacial thermal resistances between ultrathin heterointerfaces and top and bottom metallic contacts on cross-plane thermal transport.

Importantly, this work has yielded significant advancements in the epitaxial growth of high-quality heterogeneous interfaces over large areas as well as in the quantitative understanding of interfacial thermal transport across atomically thin vdW films on various substrates. The implications of these findings are extensive for the design of heat-sensitive electronic components and 2D electronic devices, such as 2D transistors and microchips, that can operate without thermal limitations, e.g., overheating. The ability to obstruct heat dissipation in the vertical direction while maintaining in-plane crystallinity in wafer-scale engineered vdW stacks not only facilitates thermal management applications but also enhances their suitability as active materials in thermoelectric devices. Combining with bandgap engineering strategies and careful selection of materials with compatible thermal expansion coefficients to avoid strain, the followed phonon engineering approach could provide a promising route to realize a wide variety of functional semiconductor heterojunctions and superlattices for nanoscale electronic and thermoelectric devices.

■ ASSOCIATED CONTENT

Supporting Information

The Supporting Information is available free of charge at https://pubs.acs.org/doi/10.1021/acs.nanolett.3c01280.

RHEED patterns; XPS spectra; FDTR sensitivity analysis; FDTR experimental data; Raman experimental data; tight-binding phonon calculations; experimental and computational methods (PDF)

■ AUTHOR INFORMATION

Corresponding Author

Alexandros El Sachat − *Catalan Institute of Nanoscience and Nanotechnology (ICN2), Barcelona 08193, Spain; Institute of Nanoscience and Nanotechnology, National Center for Scientific Research "Demokritos", Athens 15341, Greece;* Email: a.elsachat@inn.demokritos.gr

Authors

Emigdio Chavez-Angel − *Catalan Institute of Nanoscience and Nanotechnology (ICN2), Barcelona 08193, Spain;* orcid.org/0000-0002-9783-0806

Polychronis Tsipas − *Institute of Nanoscience and Nanotechnology, National Center for Scientific Research "Demokritos", Athens 15341, Greece;* orcid.org/0000-0001-9064-9601

Peng Xiao − *Catalan Institute of Nanoscience and Nanotechnology (ICN2), Barcelona 08193, Spain;* orcid.org/0000-0002-4711-2566

Mohammad Taghi Ahmadi − *School of Engineering, University of Warwick, Coventry CV4 7AL, United Kingdom*

Abdalghani H. S. Daaoub − *School of Engineering, University of Warwick, Coventry CV4 7AL, United Kingdom*

Hatef Sadeghi − *School of Engineering, University of Warwick, Coventry CV4 7AL, United Kingdom;* orcid.org/0000-0001-5398-8620

Clivia M. Sotomayor Torres − *Catalan Institute of Nanoscience and Nanotechnology (ICN2), Barcelona 08193, Spain; ICREA, Barcelona 08010, Spain;* orcid.org/0000-0001-9986-2716

Athanasios Dimoulas − *Institute of Nanoscience and Nanotechnology, National Center for Scientific Research "Demokritos", Athens 15341, Greece;* orcid.org/0000-0003-3199-1356

Complete contact information is available at: https://pubs.acs.org/10.1021/acs.nanolett.3c01280

Author Contributions

A.E. conceived and supervised the research work. P.T. and A.D. fabricated the MBE samples, performed the XPS measurements, and provided inputs in the structural analysis. A.E., E.C.-A., and P.X. performed the Raman and TEM measurements and analysis. A.E. and E.C.-A. built the FDTR setup and performed the thermal measurements and data analysis. M.T.A., A.D., and H.S. performed the thermal conductance calculations and provided support to the theoretical analysis. All authors reviewed and edited the manuscript and have given approval to the final version of the manuscript. The manuscript was written by A.E. with inputs from E.C.-A., P.T., H.S., and C.M.S.T.

Notes

The authors declare no competing financial interest.

■ ACKNOWLEDGMENTS

A.E. acknowledges funding from the EU-H2020 research and innovation program under the Marie Sklodowska Curie Individual Fellowship THERMIC (Grant No. 101029727). H.S. acknowledges the UKRI for Future Leaders Fellowship numbers MR/S015329/2 and MR/X015181/1. E.C.A. and C.M.S.T. acknowledge support from the project LEIT funded by the European Research Council, H2020 Grant Agreement No. 885689. ICN2 is supported by the Severo Ochoa program from the Spanish Research Agency (AEI, grant no. SEV-2017-0706) and by the CERCA Programme/Generalitat de Catalunya. The authors acknowledge Prof. Aaron Schmidt for sharing the numerical code for the FDTR analysis.

■ REFERENCES

(1) Jin, G.; Lee, C.-S.; Okello, O. F. N.; Lee, S.-H.; Park, M. Y.; Cha, S.; Seo, S.-Y.; Moon, G.; Min, S. Y.; Yang, D.-H.; Han, C.; Ahn, H.;

Lee, J.; Choi, H.; Kim, J.; Choi, S.-Y.; Jo, M.-H. Heteroepitaxial van der Waals semiconductor superlattices. *Nat. Nanotechnol.* **2021**, *16* (10), 1092−1098.
(2) Zhao, B.; Wan, Z.; Liu, Y.; Xu, J.; Yang, X.; Shen, D.; Zhang, Z.; Guo, C.; Qian, Q.; Li, J.; Wu, R.; Lin, Z.; Yan, X.; Li, B.; Zhang, Z.; Ma, H.; Li, B.; Chen, X.; Qiao, Y.; Shakir, I.; Almutairi, Z.; Wei, F.; Zhang, Y.; Pan, X.; Huang, Y.; Ping, Y.; Duan, X.; Duan, X. High-order superlattices by rolling up van der Waals heterostructures. *Nature* **2021**, *591* (7850), 385−390.
(3) Jiang, J.; Bitla, Y.; Huang, C.-W.; Do, T. H.; Liu, H.-J.; Hsieh, Y.-H.; Ma, C.-H.; Jang, C.-Y.; Lai, Y.-H.; Chiu, P.-W.; et al. Flexible ferroelectric element based on van der Waals heteroepitaxy. *Sci. Adv.* **2017**, *3* (6), No. e1700121.
(4) Ryu, Y. K.; Frisenda, R.; Castellanos-Gomez, A. Superlattices based on van der Waals 2D materials. *Chem. Commun.* **2019**, *55* (77), 11498−11510.
(5) Merrill, D. R.; Moore, D. B.; Bauers, S. R.; Falmbigl, M.; Johnson, D. C. Misfit Layer Compounds and Ferecrystals: Model Systems for Thermoelectric Nanocomposites. *Mater.* **2015**, *8* (4), 2000−2029.
(6) Jood, P.; Ohta, M.; Nishiate, H.; Yamamoto, A.; Lebedev, O. I.; Berthebaud, D.; Suekuni, K.; Kunii, M. Microstructural Control and Thermoelectric Properties of Misfit Layered Sulfides (LaS)1+mTS2 (T = Cr, Nb): The Natural Superlattice Systems. *Chem. Mater.* **2014**, *26* (8), 2684−2692.
(7) Guo, R.; Jho, Y.-D.; Minnich, A. J. Coherent control of thermal phonon transport in van der Waals superlattices. *Nanoscale* **2018**, *10* (30), 14432−14440.
(8) Sood, A.; Sievers, C.; Shin, Y. C.; Chen, V.; Chen, S.; Smithe, K. K. H.; Chatterjee, S.; Donadio, D.; Goodson, K. E.; Pop, E. Engineering Thermal Transport across Layered Graphene-MoS2 Superlattices. *ACS Nano* **2021**, *15* (12), 19503−19512.
(9) Chen, G.; Neagu, M. Thermal conductivity and heat transfer in superlattices. *Appl. Phys. Lett.* **1997**, *71* (19), 2761−2763.
(10) Kim, S. E.; Mujid, F.; Rai, A.; Eriksson, F.; Suh, J.; Poddar, P.; Ray, A.; Park, C.; Fransson, E.; Zhong, Y.; Muller, D. A.; Erhart, P.; Cahill, D. G.; Park, J. Extremely anisotropic van der Waals thermal conductors. *Nature* **2021**, *597* (7878), 660−665.
(11) Lin, Z.; Wan, Z.; Song, F.; Huang, B.; Jia, C.; Qian, Q.; Kang, J. S.; Wu, Y.; Yan, X.; Peng, L.; Wan, C.; Zhou, J.; Sofer, Z.; Shakir, I.; Almutairi, Z.; Tolbert, S.; Pan, X.; Hu, Y.; Huang, Y.; Duan, X. High-yield exfoliation of 2D semiconductor monolayers and reassembly of organic/inorganic artificial superlattices. *Chem.* **2021**, *7* (7), 1887−1902.
(12) Wang, C.; He, Q.; Halim, U.; Liu, Y.; Zhu, E.; Lin, Z.; Xiao, H.; Duan, X.; Feng, Z.; Cheng, R.; et al. Monolayer atomic crystal molecular superlattices. *Nature* **2018**, *555* (7695), 231−236.
(13) Vaziri, S.; Yalon, E.; Muñoz Rojo, M.; Suryavanshi, S. V.; Zhang, H.; McClellan, C. J.; Bailey, C. S.; Smithe, K. K. H.; Gabourie, A. J.; Chen, V.; et al. Ultrahigh thermal isolation across heterogeneously layered two-dimensional materials. *Sci. Adv.* **2019**, *5* (8), No. eaax1325.
(14) Lin, M.; Wu, D.; Zhou, Y.; Huang, W.; Jiang, W.; Zheng, W.; Zhao, S.; Jin, C.; Guo, Y.; Peng, H.; Liu, Z. Controlled Growth of Atomically Thin In2Se3 Flakes by van der Waals Epitaxy. *J. Am. Chem. Soc.* **2013**, *135* (36), 13274−13277.
(15) Koma, A. Van der Waals epitaxy—a new epitaxial growth method for a highly lattice-mismatched system. *Thin Solid Films* **1992**, *216* (1), 72−76.
(16) Ravichandran, J.; Yadav, A. K.; Cheaito, R.; Rossen, P. B.; Soukiassian, A.; Suresha, S. J.; Duda, J. C.; Foley, B. M.; Lee, C.-H.; Zhu, Y.; Lichtenberger, A. W.; Moore, J. E.; Muller, D. A.; Schlom, D. G.; Hopkins, P. E.; Majumdar, A.; Ramesh, R.; Zurbuchen, M. A. Crossover from incoherent to coherent phonon scattering in epitaxial oxide superlattices. *Nat. Mater.* **2014**, *13* (2), 168−172.
(17) Nunn, W.; Truttmann, T. K.; Jalan, B. A review of molecular-beam epitaxy of wide bandgap complex oxide semiconductors. *J. Mater. Res.* **2021**, *36* (23), 4846−4864.
(18) Saleta Reig, D.; Varghese, S.; Farris, R.; Block, A.; Mehew, J. D.; Hellman, O.; Woźniak, P.; Sledzinska, M.; El Sachat, A.; Chávez-Ángel, E.; et al. Unraveling Heat Transport and Dissipation in Suspended MoSe2 from Bulk to Monolayer. *Adv. Mater.* **2022**, *34* (10), 2108352.
(19) Fournier, D.; Marangolo, M.; Eddrief, M.; Kolesnikov, N. N.; Fretigny, C. Straightforward measurement of anisotropic thermal properties of a Bi_2Se_3 single crystal. *J. Phys.: Condens. Matter* **2018**, *30* (11), 115701.
(20) Paulatto, L.; Fournier, D.; Marangolo, M.; Eddrief, M.; Atkinson, P.; Calandra, M. Thermal conductivity of Bi2Se3 from bulk to thin films: Theory and experiment. *Phys. Rev. B* **2020**, *101* (20), 205419.
(21) Chen, L.; Zhang, W.; Zhang, H.; Chen, J.; Tan, C.; Yin, S.; Li, G.; Zhang, Y.; Gong, P.; Li, L. In-Plane Anisotropic Thermal Conductivity of Low-Symmetry PdSe2. *Sustainability* **2021**, *13* (8), 4155.
(22) Jena, T.; Hossain, M. T.; Giri, P. K. Temperature-dependent Raman study and determination of anisotropy ratio and in-plane thermal conductivity of low-temperature CVD-grown PdSe2 using unpolarized laser excitation. *J. Mater. Chem. C* **2021**, *9* (46), 16693−16708.
(23) Tsipas, P.; Xenogiannopoulou, E.; Kassavetis, S.; Tsoutsou, D.; Golias, E.; Bazioti, C.; Dimitrakopulos, G. P.; Komninou, P.; Liang, H.; Caymax, M.; Dimoulas, A. Observation of Surface Dirac Cone in High-Quality Ultrathin Epitaxial Bi2Se3 Topological Insulator on AlN(0001) Dielectric. *ACS Nano* **2014**, *8* (7), 6614−6619.
(24) Tsipas, P.; Tsoutsou, D.; Marquez-Velasco, J.; Aretouli, K. E.; Xenogiannopoulou, E.; Vassalou, E.; Kordas, G.; Dimoulas, A. Epitaxial ZrSe2/MoSe2 semiconductor v.d. Waals heterostructures on wide band gap AlN substrates. *Microelectron. Eng.* **2015**, *147*, 269−272.
(25) Le, P. H.; Wu, K. H.; Luo, C. W.; Leu, J. Growth and characterization of topological insulator Bi2Se3 thin films on SrTiO3 using pulsed laser deposition. *Thin Solid Films* **2013**, *534*, 659−665.
(26) Zhang, J.; Peng, Z.; Soni, A.; Zhao, Y.; Xiong, Y.; Peng, B.; Wang, J.; Dresselhaus, M. S.; Xiong, Q. Raman Spectroscopy of Few-Quintuple Layer Topological Insulator Bi2Se3 Nanoplatelets. *Nano Lett.* **2011**, *11* (6), 2407−2414.
(27) Tonndorf, P.; Schmidt, R.; Böttger, P.; Zhang, X.; Börner, J.; Liebig, A.; Albrecht, M.; Kloc, C.; Gordan, O.; Zahn, D. R. T.; Michaelis de Vasconcellos, S.; Bratschitsch, R. Photoluminescence emission and Raman response of monolayer MoS2, MoSe2, and WSe2. *Opt. Express* **2013**, *21* (4), 4908−4916.
(28) Varghese, S.; Saleta Reig, D.; Dudley Mehew, J.; Block, A.; El Sachat, A.; Chávez-Ángel, E.; Sledzinska, M.; Ballesteros, B.; Sotomayor Torres, C. M.; Tielrooij, K.-J. Fabrication and characterization of large-area suspended $MoSe_2$ crystals down to the monolayer. *J. Phys. Chem. Mater.* **2021**, *4* (4), 046001.
(29) Li, Z.; Peng, B.; Lin, M.-L.; Leng, Y.-C.; Zhang, B.; Pang, C.; Tan, P.-H.; Monserrat, B.; Chen, F. Phonon-assisted electronic states modulation of few-layer PdSe2 at terahertz frequencies. *npj 2D Mater. Appl.* **2021**, *5* (1), 87.
(30) Wei, M.; Lian, J.; Zhang, Y.; Wang, C.; Wang, Y.; Xu, Z. Layer-dependent optical and dielectric properties of centimeter-scale PdSe2 films grown by chemical vapor deposition. *npj 2D Mater. Appl.* **2022**, *6* (1), 1.
(31) Yu, J.; Kuang, X.; Gao, Y.; Wang, Y.; Chen, K.; Ding, Z.; Liu, J.; Cong, C.; He, J.; Liu, Z.; Liu, Y. Direct Observation of the Linear Dichroism Transition in Two-Dimensional Palladium Diselenide. *Nano Lett.* **2020**, *20* (2), 1172−1182.
(32) Yang, H.; Xiao, Y.; Zhang, K.; Chen, Z.; Pan, J.; Zhuo, L.; Zhong, Y.; Zheng, H.; Zhu, W.; Yu, J.; Chen, Z. Self-powered and high-performance all-fiber integrated photodetector based on graphene/palladium diselenide heterostructures. *Opt. Express* **2021**, *29* (10), 15631−15640.
(33) Bauer, M.; Gigler, A. M.; Huber, A. J.; Hillenbrand, R.; Stark, R. W. Temperature-depending Raman line-shift of silicon carbide. *J. Raman. Spectrosc.* **2009**, *40* (12), 1867−1874.

https://doi.org/10.1021/acs.nanolett.3c01280
Nano Lett. 2023, 23, 6883−6891

(34) El Sachat, A.; Xiao, P.; Donadio, D.; Bonell, F.; Sledzinska, M.; Marty, A.; Vergnaud, C.; Boukari, H.; Jamet, M.; Arregui, G.; et al. Effect of crystallinity and thickness on thermal transport in layered PtSe2. *npj 2D Mater. Appl.* **2022**, *6* (1), 32.
(35) Xiao, P.; Chavez-Angel, E.; Chaitoglou, S.; Sledzinska, M.; Dimoulas, A.; Sotomayor Torres, C. M.; El Sachat, A. Anisotropic Thermal Conductivity of Crystalline Layered SnSe2. *Nano Lett.* **2021**, *21* (21), 9172−9179.
(36) Schmidt, A. J.; Cheaito, R.; Chiesa, M. A frequency-domain thermoreflectance method for the characterization of thermal properties. *Rev. Sci. Instrum.* **2009**, *80* (9), 094901.
(37) Landolt-Börnstein−Group III Condensed Matter: Bismuth selenide (Bi_2Se_3) Debye temperature, heat capacity. In *Non-Tetrahedrally Bonded Elements and Binary Compounds I*; Springer; Vol. 41C. DOI: 10.1007/10681727_948
(38) Kiwia, H. L.; Westrum, E. F. Low-temperature heat capacities of molybdenum diselenide and ditelluride. *J. Chem. Thermodyn.* **1975**, *7* (7), 683−691.
(39) Schmidt, A. J.; Chen, X.; Chen, G. Pulse accumulation, radial heat conduction, and anisotropic thermal conductivity in pump-probe transient thermoreflectance. *Rev. Sci. Instrum.* **2008**, *79* (11), 114902.
(40) Koh, Y. K.; Cao, Y.; Cahill, D. G.; Jena, D. Heat-Transport Mechanisms in Superlattices. *Adv. Funct. Mater.* **2009**, *19* (4), 610−615.
(41) Cheaito, R.; Duda, J. C.; Beechem, T. E.; Hattar, K.; Ihlefeld, J. F.; Medlin, D. L.; Rodriguez, M. A.; Campion, M. J.; Piekos, E. S.; Hopkins, P. E. Experimental Investigation of Size Effects on the Thermal Conductivity of Silicon-Germanium Alloy Thin Films. *Phys. Rev. Lett.* **2012**, *109* (19), 195901.
(42) Chalopin, Y.; Esfarjani, K.; Henry, A.; Volz, S.; Chen, G. Thermal interface conductance in Si/Ge superlattices by equilibrium molecular dynamics. *Phys. Rev. B* **2012**, *85* (19), 195302.
(43) Chen, Y.; Li, D.; Lukes, J. R.; Ni, Z.; Chen, M. Minimum superlattice thermal conductivity from molecular dynamics. *Phys. Rev. B* **2005**, *72* (17), 174302.
(44) Sood, A.; Xiong, F.; Chen, S.; Cheaito, R.; Lian, F.; Asheghi, M.; Cui, Y.; Donadio, D.; Goodson, K. E.; Pop, E. Quasi-Ballistic Thermal Transport Across MoS2 Thin Films. *Nano Lett.* **2019**, *19* (4), 2434−2442.
(45) Li, X.; Yang, R. Effect of lattice mismatch on phonon transmission and interface thermal conductance across dissimilar material interfaces. *Phys. Rev. B* **2012**, *86* (5), 054305.
(46) Touzelbaev, M. N.; Zhou, P.; Venkatasubramanian, R.; Goodson, K. E. Thermal characterization of Bi2Te3/Sb2Te3 superlattices. *J. Appl. Phys.* **2001**, *90* (2), 763−767.
(47) Islam, M. S.; Mia, I.; Islam, A. S. M. J.; Stampfl, C.; Park, J. Temperature and interlayer coupling induced thermal transport across graphene/2D-SiC van der Waals heterostructure. *Sci. Rep.* **2022**, *12* (1), 761.
(48) Islam, M. S.; Mia, I.; Ahammed, S.; Stampfl, C.; Park, J. Exceptional in-plane and interfacial thermal transport in graphene/2D-SiC van der Waals heterostructures. *Sci. Rep.* **2020**, *10* (1), 22050.
(49) Koh, Y. K.; Bae, M.-H.; Cahill, D. G.; Pop, E. Heat Conduction across Monolayer and Few-Layer Graphenes. *Nano Lett.* **2010**, *10* (11), 4363−4368.
(50) Sadeghi, H. Theory of electron, phonon and spin transport in nanoscale quantum devices. *Nanotechnology* **2018**, *29* (37), 373001.
(51) Xiao, Y.; He, S.; Li, M.; Sun, W.; Wu, Z.; Dai, W.; Lu, C. Structural evolution and phase transition mechanism of $MoSe_2$ under high pressure. *Sci. Rep.* **2021**, *11* (1), 22090.
(52) Wang, B.-T.; Zhang, P. Phonon spectrum and bonding properties of Bi2Se3: Role of strong spin-orbit interaction. *Appl. Phys. Lett.* **2012**, *100* (8), 082109.

https://doi.org/10.1021/acs.nanolett.3c01280
Nano Lett. 2023, 23, 6883−6891